Quasi-static crack propagation with a Griffith criterion using a discrete element method

Frédéric Marazzato, Alexandre Ern, Laurent Monasse

Frédéric Marazzato, Alexandre Ern, Laurent Monasse. Quasi-static crack propagation with a Griffith criterion using a discrete element method. 2021. hal-03102982v1

HAL Id: hal-03102982
https://hal.science/hal-03102982v1

Preprint submitted on 7 Jan 2021 (v1), last revised 21 Oct 2021 (v3)

Quasi-static crack propagation with a Griffith criterion using a discrete element method

Frédéric Marazzato[1,2,3], Alexandre Ern[2,3] and Laurent Monasse[4]
[1]Department of Mathematics, Louisiana State University, Baton Rouge, LA 70803, USA
email: `marazzato@lsu.edu`
[2]CERMICS, Ecole des Ponts, 77455 Marne-la-Vallée, France
email: `alexandre.ern@enpc.fr`
[3]Inria, 2 rue Simone Iff, 75589 Paris, France
[4]Université Côte d'Azur, Inria, CNRS, LJAD, EPC COFFEE, 06108 Nice, France
email: `laurent.monasse@inria.fr`

Abstract

A variational discrete element method is applied to simulate quasi-static crack propagation. Cracks are considered to propagate between the mesh cells through the mesh facets. The elastic behaviour is parametrized by the continuous mechanical parameters (Young modulus and Poisson ratio). A discrete energetic cracking criterion coupled to a discrete kinking criterion guide the cracking process. Two-dimensional numerical examples are presented to illustrate the robustness and versatility of the method.

1 Introduction

Discrete element methods (DEM) are popular in the modelling of granular materials, soil and rock mechanics. DEM generally use sphere packing to discretize the domain as small spheres interacting through forces and torques [20], but the main difficulty is to derive a suitable set of parameter values for those interactions so as to reproduce a given Young modulus E and Poisson ratio ν at the macroscopic level [18, 8]. Advantages of DEM are their ability to deal with discontinuous materials, such as fractured or porous materials, as well as the possibility to take advantage of GPU computations [30]. A first DEM parametrized only by E and ν has been proposed in [25] for elastic computations on Voronoi meshes. In a consecutive work [22], a consistent DEM has been proposed for elasto-plasticity computations on polyhedral meshes using cell-wise reconstructions of the strains.

DEM for cracking have been developed in [3] and [2] with cracks propagating through the facets of the (Voronoi) mesh and using a critical stress criterion (initiation criterion). A similar approach, but using a different reconstruction of strains based on moving least-squares interpolations, can be traced back to [5] (2d) and [31] (3d). Crack propagation can be based instead on the Griffith criterion which relies on the computation of the stress intensity factors (SIF) at the crack tip when coupled with the Irwin formula. Virtual element methods (VEM) have been recently applied to crack propagation [17]. Cracks were allowed to cut through the polyhedral mesh cells as in the extended finite element method (XFEM) which is based on an extended space of basis functions [9] and a level-set description of the crack [24]. Phase-field methods instead smooth the crack and have been developed among others in [7] and subsequent work. Phase-field methods are not based on SIF computations but rather on a variational formulation of cracking [14]. Furthermore DEM using cohesive laws have been developed for fragmentation computations [23] with a view towards uniting initiation and propagation. These methods allow one to devise an initiation criterion and also to control the energy dissipation as with a Griffith criterion. The cracks still go through the mesh facets. This is also the case for similar methods of higher-order such as discontinuous Galerkin methods [15].

The main goal of the present work is to develop a consistent DEM on polyhedral meshes using a Griffith criterion to compute crack propagation through the mesh facets. The proposed method is close to [22] (where there is no cracking) but the degrees of freedom (dofs) are different. In addition to the usual dofs attached to the mesh cells, we use displacement dofs attached to the Dirichlet boundary rather than dofs attached to the entire boundary. The reason for removing the dofs at the Neumann boundary is to simplify the cracking procedure as no dof has to be created when an inner facet cracks. The cracking algorithm hinges on two main ingredients. The first ingredient is an approximation of the energy release rate at every vertex along the crack. The second ingredient is a kinking criterion used to determine the next breaking facet and thus the crack path. The kinking criterion, in the spirit of [28], consists in selecting for the crack path the inner facet of the mesh that maximizes a quantity representing the local density of elastic energy.

The present work is organized as follows. Section 2 briefly recalls the equations of elasticity and cracking in a Cauchy continuum. Section 3 introduces the proposed DEM and presents the space discretization of the governing equations. Moreover a numerical test is reported to assess the convergence of the space discretization in the presence of a singularity. Section 4 addresses the full discretization of the quasi-static cracking problem. Section 5 contains numerical results on quasi-static crack propagation problems in two space dimensions. Finally, Section 6 draws some conclusions.

2 Governing equations for quasi-static cracking

We consider an elastic fragile material occupying the domain $\Omega \subset \mathbb{R}^2$ in the reference configuration and evolving over the finite pseudo-time interval $[0, T]$, $T > 0$, under the action of a volumetric force f and boundary conditions. The pseudo-time interval $[0, T]$ is discretized by means of $(K + 1)$ discrete pseudo-time nodes $(t_k)_{k\in\{0,\dots,K\}}$ with $t_0 := 0$ and $t_N := T$. The strain regime is restricted to small strains so that we use the linearized strain tensor $\varepsilon(u) := \frac{1}{2}(\nabla u + (\nabla u)^{\mathsf{T}}) \in \mathbb{R}^{2\times 2}$, where u is the $\mathbb{R}^2$–valued displacement field. The material is supposed to be homogeneous and isotropic. The stress tensor $\sigma(u) \in \mathbb{R}^{2\times 2}$ is such that

$$\sigma(u) := \mathbb{C} : \varepsilon(u), \tag{1}$$

where $\mathbb{C}$ is the fourth-order stiffness tensor. The elastic material is characterized by the Young modulus E and the Poisson ratio ν or equivalently by the Lamé coefficients λ and μ. The boundary of Ω is partitioned as $\partial\Omega = \partial\Omega_D \cup \partial\Omega_N$, a Dirichlet condition is prescribed on $\partial\Omega_D$, and a Neumann condition on $\partial\Omega_N$, so that we enforce for all $k = 0, \cdots, K$,

$$u = u_D(t_k) \ \text{ on } \partial\Omega_D, \qquad \sigma(u)\cdot n = g_N(t_k) \ \text{ on } \partial\Omega_N. \tag{2}$$

Since cracking can occur, we denote $\Gamma(t_k)$ the crack at the pseudo-time t_k and the actual domain at the pseudo-time t_k is

$$\Omega(t_k) := \Omega \setminus \Gamma(t_k). \tag{3}$$

This implies that $\partial\Omega(t_k) = \partial\Omega_D \cup \partial\Omega_N \cup \Gamma(t_k)$. We enforce a homogeneous Neumann condition on $\Gamma(t_k)$ for all $k = 0, \cdots, K$, i.e.,

$$\sigma(u)\cdot n = 0 \ \text{ on } \Gamma(t_k). \tag{4}$$

Since we are interested in crack propagation, we assume that $\Omega(0)$ already contains a crack, i.e., $\Gamma(0) \neq \emptyset$. The crack $\Gamma(t_k)$ is supposed to be a countably rectifiable 1–manifold for all $k = 0, \cdots, K$ (see [10]). This hypothesis ensures the almost everywhere (a.e.) existence of a normal vector n and a tangent vector τ to $\Gamma(t_k)$ at any point $y \in \Gamma(t_k)$ [29].

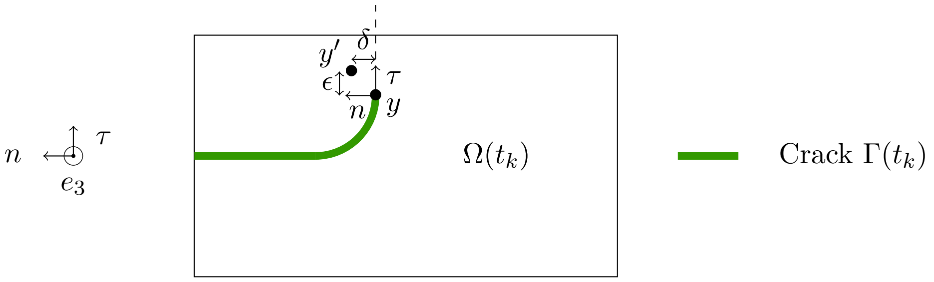

Figure 1: Sketch of a crack in the two-dimensional domain $\Omega(t_k)$.

The stress intensity factors (SIF) at any point $y \in \Gamma(t_k)$ are usually defined for a purely elastic material as

$$\begin{cases} K_1(y) := \lim\limits_{\delta\downarrow 0, \epsilon\to 0} \sigma_{nn}(y')\sqrt{2\pi d(y,y')}, \\ K_2(y) := \lim\limits_{\delta\downarrow 0, \epsilon\to 0} \sigma_{n\tau}(y')\sqrt{2\pi d(y,y')}, \end{cases} \tag{5}$$

where $d(\cdot,\cdot)$ is the Euclidean distance in $\mathbb{R}^2$ and $y' := y + \delta n + \epsilon\tau$ (see Figure 1). If the stresses remain bounded in the vicinity of $y \in \Gamma(t_k)$, then the SIF are null. Using the Irwin formula, one can define the energy release rate $\mathcal{G}(y)$ in the plane strain hypothesis as

$$\mathcal{G}(y) := \frac{1-\nu^2}{E}\left(K_1(y)^2 + K_2(y)^2\right). \tag{6}$$

Admissible states are characterized by the inequality

$$\mathcal{G}(y) \le \mathcal{G}_c, \quad \forall y \in \Gamma(t_k), \tag{7}$$

where $\mathcal{G}_c$ is a material property associated with the capacity of the material to sustain loads without locally failing and thus opening cracks. The material remains healthy at the point $y \in \Gamma(t_k)$ if $\mathcal{G}(y) < \mathcal{G}_c$ and breaks if $\mathcal{G}(y) = \mathcal{G}_c$. The material parameter $\mathcal{G}_c$ is assumed to be homogeneous for simplicity.

To formulate the governing equations for quasi-static cracking, we consider the following functional spaces depending on the pseudo-time node t_k:

$$V_D(t_k) := \left\{v \in H^1(\Omega(t_k);\mathbb{R}^d) \mid v_{|\partial\Omega_D} = u_D(t_k)\right\}, \qquad V_0(t_k) := \left\{v \in H^1(\Omega(t_k);\mathbb{R}^d) \mid v_{|\partial\Omega_D} = 0\right\}, \tag{8}$$

where standard notation is used for the Hilbert Sobolev spaces. The weak solution is searched as a pair (u,Γ) such that for all $k = 0,\cdots,K$, $u(t_k) \in V_D(t_k)$, $\Gamma(t_k) \subset \Omega$ is a 1–manifold satisfying the above assumptions, and

$$\begin{cases} a(t_k; u(t_k), \tilde{v}) = l(t_k;\tilde{v}), & \forall \tilde{v} \in V_0(t_k), \\ \mathcal{G}(y) \le \mathcal{G}_c, & \forall y \in \Gamma(t_k). \end{cases} \tag{9}$$

Here we introduced the stiffness bilinear form such that for all $(v,\tilde{v}) \in V_D(t_k)\times V_0(t_k)$,

$$a(t_k; v, \tilde{v}) := \int_{\Omega(t_k)} \varepsilon(v) : \mathbb{C} : \varepsilon(\tilde{v}), \tag{10}$$

and the linear form acting on $V_0(t_k)$ as follows:

$$l(t_k;\tilde{v}) := \int_{\Omega(t_k)} f(t_k)\cdot\tilde{v} + \int_{\partial\Omega_N} g_N(t_k)\cdot\tilde{v}. \tag{11}$$

Note that the Dirichlet condition on $\partial\Omega_D$ is enforced strongly, whereas the Neumann condition on $\partial\Omega_N \cup \Gamma(t_k)$ is enforced weakly.

3 Space semi-discretization

In this section we present the space semi-discretization of (9) using a DEM.

3.1 Discrete sets and degrees of freedom

The domain Ω is discretized with a mesh $\mathcal{T}_h$ of size h made of polygons with straight edges. We assume that Ω is itself a polygon so that the mesh covers Ω exactly. We also assume that the mesh is compatible with the initial crack position $\Gamma(0)$ and with the partition of the boundary into the Dirichlet and Neumann parts.

Let $\mathcal{C}$ denote the set composed of the mesh cells and, for all $k = 0, \dots, K$, let $\mathcal{F}(t_k)$ denote the set composed of the mesh facets. This set depends on the pseudo-time node t_k since a facet $F \in \mathcal{F}(t_k)$ is replaced, after cracking, by two boundary facets $F_-, F_+ \in \mathcal{F}(t_k)$ (F_-, F_+ are the same geometric object, but are different objects regarding the data structure since each one belongs to the boundary of a different mesh cell). We partition the set of mesh facets as $\mathcal{F}(t_k) = \mathcal{F}^i(t_k) \cup \mathcal{F}^b(t_k)$, where $\mathcal{F}^i(t_k)$ is composed of the internal facets shared by two mesh cells and $\mathcal{F}^b(t_k)$ is the collection of the boundary facets sitting on the boundary $\partial\Omega(t_k) = \partial\Omega_D \cup \partial\Omega_N \cup \Gamma(t_k)$ (notice that such facets belong to the boundary of only one mesh cell). The subsets $\mathcal{F}^i(t_k)$ and $\mathcal{F}^b(t_k)$ depend on the pseudo-time node t_k since, as the facet $F \in \mathcal{F}^i(t_k)$ cracks, it is replaced by the facets $F_+, F_- \in \mathcal{F}^b(t_k)$. For all $k = 0, \cdots, K$, the discrete crack is denoted $\Gamma_h(t_k)$ and is composed of facets belonging to a subset of $\mathcal{F}^b(t_k)$. This subset is denoted $\mathcal{F}^\Gamma(t_k) \subset \mathcal{F}^b(t_k)$. We also introduce the partition between boundary facets with Neumann boundary conditions $\mathcal{F}^b_N(t_k)$ (recall that homogeneous Neumann boundary conditions are imposed on newly created crack lips) and with Dirichlet boundary conditions $\mathcal{F}^b_D$ which does not depend on t_k. One thus has $\mathcal{F}^b(t_k) = \mathcal{F}^b_N(t_k) \cup \mathcal{F}^b_D$.

Vector-valued volumetric degrees of freedom (dofs) for a generic displacement field $v_\mathcal{C} := (v_c)_{c\in\mathcal{C}} \in \mathbb{R}^{d\#(\mathcal{C})}$ are placed at the barycentre of every mesh cell $c \in \mathcal{C}$. Additional displacement boundary dofs $v_{\mathcal{F}^b_D} := (v_F)_{F\in\mathcal{F}^b_D} \in \mathbb{R}^{d\#(\mathcal{F}^b_D)}$ are added at the barycentre of every boundary facet lying on $\partial\Omega_D$. We use the compact notation $v_h := (v_\mathcal{C}, v_{\mathcal{F}^b_D})$ for the collection of all the cell dofs and all the Dirichlet boundary facet dofs and we write $v_h \in V_h := \mathbb{R}^{d\#(\mathcal{C})} \times \mathbb{R}^{d\#(\mathcal{F}^b_D)}$. Figure 2 illustrates the position of the displacement dofs. The barycentre of a mesh cell $c \in \mathcal{C}$ is denoted by $\mathbf{x}_c$ and the barycentre of a mesh facet $F \in \mathcal{F}$ is denoted by $\mathbf{x}_F$.

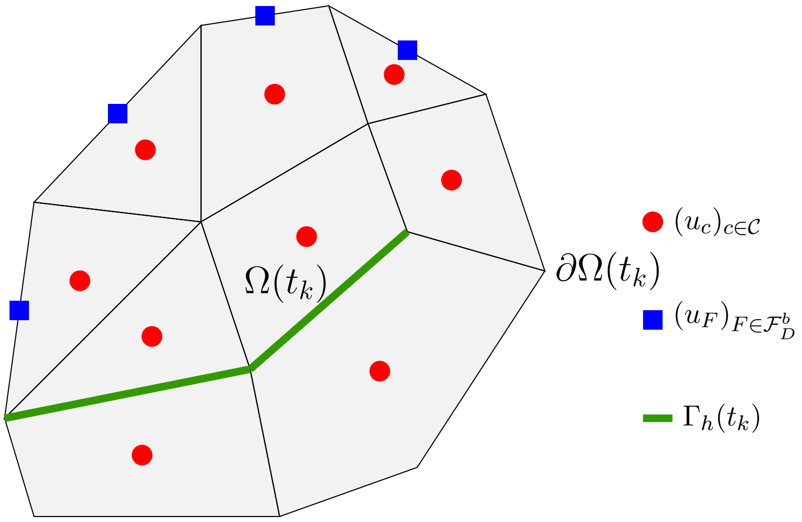

Figure 2: Domain $\Omega(t_k)$ covered by a polygonal mesh and vector-valued degrees of freedom for the displacement.

3.2 Discrete bilinear and linear forms

The discrete stiffness bilinear form hinges on a reconstruction operator that provides a displacement value at every mesh facet by an interpolation formula from neighbouring cell dofs. Specifically, using the cell and Dirichlet boundary facet dofs of $v_h \in V_h$, we reconstruct a collection of displacements $v_{\mathcal{F}} := (v_F)_{F\in\mathcal{F}(t_k)} \in \mathbb{R}^{d\#(\mathcal{F}(t_k))}$ on all the mesh facets. The reconstruction operator is denoted $\mathcal{R}(t_k;\cdot)$ and we write

$$v_{\mathcal{F}} := \mathcal{R}(t_k; v_h) \in \mathbb{R}^{d\#(\mathcal{F}(t_k))}. \tag{12}$$

The reconstruction operator depends on t_k because of the connectivity modifications due to the crack propagation.

Let us first describe the reconstruction operator on boundary facets. Let $F \in \mathcal{F}^b_D$ be a Dirichlet boundary facet. Then the reconstruction is simply defined by taking the value of the dof located at $\mathbf{x}_F$. Let $F \in \mathcal{F}^b_N(t_k)$ be a Neumann boundary facet. The main idea to define v_F is to use a barycentric combination of the cell dofs close to F. A similar idea has been considered for finite volume methods in [13, Sec. 2.2] and for cell-centered Galerkin methods in [11]. We thus select a subset of neighboring cell dofs of F, say $\mathcal{I}_F \subset \mathcal{C}$, and set

$$v_F := \sum_{i\in\mathcal{I}_F} \alpha_i(\mathbf{x}_F)v_i, \tag{13}$$

where the v_i's are the dofs of v_h and the coefficients $\alpha_i(\mathbf{x}_F)$ are the barycentric coordinates of the facet barycenter $\mathbf{x}_F$ in terms of the selected positions of the dofs. For this construction to be meaningful, the points associated with the selected dofs must not lie on the same hyperplane, so that, in particular, the cardinality of $\mathcal{I}_F$ is at least $(d+1)$.

Let us then describe the reconstruction for an inner facet $F \in \mathcal{F}^i(t_k)$. We use a reconstruction similar to the one presented above except that the two cells sharing the inner facet F play symmetric roles. We refer to this construction as symmetric reconstruction. Specifically, let c_+ and c_- be the two cells sharing the inner facet $F \in \mathcal{F}^i(t_k)$. Then, we select $\mathcal{I}_-$ (resp. $\mathcal{I}_+$) as being composed of the cell c_+ (resp. c_-) and of all the other cells sharing an inner facet with c_- (resp. c_+), and we set

$$v_F := \frac{1}{2}\sum_{i\in\mathcal{I}_-\cup\mathcal{I}_+} \alpha_i(\mathbf{x}_F)v_i, \tag{14}$$

so that, in the case of a simplicial mesh, $2(d+1)$ dofs are used for the reconstruction (always including c_- and c_+). Note that $\sum_{i\in\mathcal{I}_-}\alpha_i(\mathbf{x}_F) = \sum_{i\in\mathcal{I}_+}\alpha_i(\mathbf{x}_F) = 1$ here. Figure 3 presents an example where $c_- = c_i$, $c_+ = c_j$, $\mathcal{I}_- = \{j, j_2, j_3\}$ and $\mathcal{I}_+ = \{i, i_2, i_3\}$.

Having defined the reconstructed facet displacements, it is now possible to devise a discrete $\mathbb{R}^{d\times d}$-valued piecewise-constant gradient field for the displacement that we write $G_{\mathcal{C}}(v_{\mathcal{F}}) := (G_c(v_{\mathcal{F}}))_{c\in\mathcal{C}} \in \mathbb{R}^{d^2\#(\mathcal{C})}$. Specifically, we set in every mesh cell $c \in \mathcal{C}$,

$$G_c(v_{\mathcal{F}}) := \sum_{F\in\partial c} \frac{|F|}{|c|} v_F \otimes n_{F,c}, \tag{15}$$

where the summation is over the facets F of c and $n_{F,c}$ is the outward normal to c on F. Note that (15) is motivated by a Stokes formula and that for all $v_h \in V_h$, we have

$$G_c(\mathcal{R}(t_k; v_h)) = \sum_{F\in\partial c} \frac{|F|}{|c|}(\mathcal{R}(t_k; v_h)_F - v_c) \otimes n_{F,c}, \tag{16}$$

since $\sum_{F\in\partial c}|F|n_{F,c} = 0$. We define a constant linearized strain tensor in every mesh cell $c \in \mathcal{C}$ such that

$$\varepsilon_c(v_{\mathcal{F}}) := \frac{1}{2}(G_c(v_{\mathcal{F}}) + G_c(v_{\mathcal{F}})^{\mathsf{T}}) \in \mathbb{R}^{d\times d}, \tag{17}$$

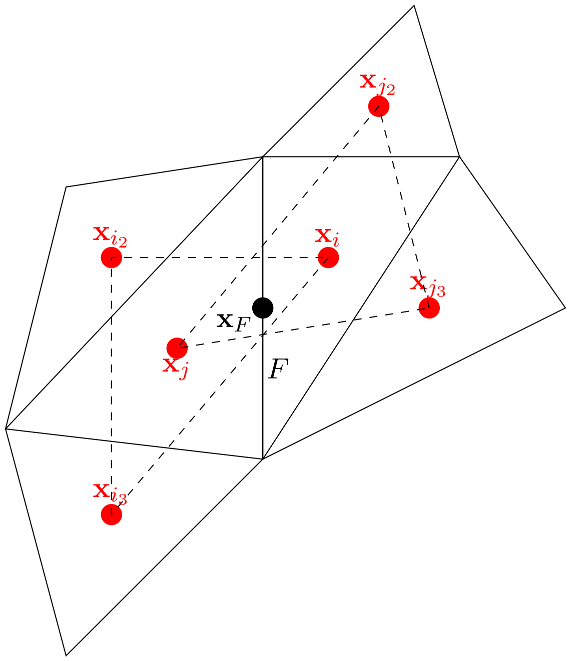

Figure 3: Dofs associated with the interior facet F used in the reconstruction.

and a constant stress tensor in every mesh cell $c \in \mathcal{C}$ such that

$$\Sigma_c(v_{\mathcal{F}}) := \mathbb{C} : \varepsilon_c(v_{\mathcal{F}}) \in \mathbb{R}^{d\times d}. \tag{18}$$

Finally, we define an additional reconstruction that is used to formulate the stabilization bilinear form in the discrete problem (see below). This operator is a cellwise nonconforming P^1 reconstruction $\mathfrak{R}_c$ defined for all $c \in \mathcal{C}$ by

$$\mathfrak{R}_c(t_k; v_h)(\mathbf{x}) := v_c + G_c(\mathcal{R}(t_k; v_h)) \cdot (\mathbf{x} - \mathbf{x}_c), \tag{19}$$

where $\mathbf{x} \in c$ and $\mathbf{x}_c$ is the barycentre of the cell c.

3.3 Discrete problem

Recalling that $V_h := \mathbb{R}^{d\#(\mathcal{C})} \times \mathbb{R}^{d\#(\mathcal{F}_D^b)}$, we set

$$\begin{cases} V_{hD}(t_k) := \{v_h \in V_h \mid v_F = u_D(t_k, \mathbf{x}_F),\ \forall F \subset \partial\Omega_D\}, \quad \forall k = 0, \cdots, K, \\ \qquad V_{h0} := \{v_h \in V_h \mid v_F = 0,\ \forall F \subset \partial\Omega_D\}. \end{cases} \tag{20}$$

The discrete stiffness bilinear form is such that for all $(v_h, \tilde{v}_h) \in V_{hD}(t_k) \times V_{h0}(t_k)$ (compare with (10))

$$a_h(t_k; v_h, \tilde{v}_h) := \sum_{c\in\mathcal{C}} |c| \varepsilon_c(\mathcal{R}(t_k; v_h)) : \mathbb{C} : \varepsilon_c(\mathcal{R}(t_k; \tilde{v}_h)) + s_h(t_k; v_h, \tilde{v}_h), \tag{21}$$

where the stabilization bilinear form s_h is intended to render a_h coercive and is defined as

$$s_h(t_k; v_h, \tilde{v}_h) = \sum_{F\in\mathcal{F}^i(t_k)} \frac{\eta}{h_F} |F| [\mathfrak{R}(t_k; v_h)]_F \cdot [\mathfrak{R}(t_k; \tilde{v}_h)]_F + \sum_{F\in\mathcal{F}_D^b} \frac{\eta}{h_F} |F| [\mathfrak{R}(t_k; v_h)]_F \cdot [\mathfrak{R}(t_k; \tilde{v}_h)]_F \tag{22}$$

where h_F is the diameter of the facet $F \in \mathcal{F}(t_k)$. For an interior facet $F \in \mathcal{F}^i(t_k)$, writing c_- and c_+ the two mesh cells sharing F, i.e., $F = \partial c_- \cap \partial c_+$, and orienting F by the unit normal vector n_F pointing from c_- to c_+, the jump of $\mathfrak{R}(t_k; v_h)$ across F is defined as

$$[\mathfrak{R}(t_k; v_h)]_F := \mathfrak{R}_{c_-}(t_k; v_h)(\mathbf{x}_F) - \mathfrak{R}_{c_+}(t_k; v_h)(\mathbf{x}_F). \tag{23}$$

The sign of the jump is irrelevant in what follows. The role of the summation over the interior facets in (22) is to penalize the jumps of the cell reconstruction $\mathfrak{R}$ across the interior facets. For a Dirichlet boundary facet $F \in \mathcal{F}_D^b$, we denote c_- the unique mesh cell containing F, we orient F by the unit normal vector $n_F := n_{c_-}$ which points outward Ω, and we define

$$[\mathfrak{R}(t_k; v_h)]_F := v_F - \mathfrak{R}_{c_-}(t_k; v_h)(\mathbf{x}_F). \tag{24}$$

The role of the summation over the Dirichlet boundary facets in (22) is to penalize the jumps between the cell reconstruction $\mathfrak{R}$ and the value reconstructed in the boundary facets. Finally, the parameter $\eta > 0$ in (22) is user-defined with the only requirement that $\eta > 0$. The bilinear form s_h is classical in the context of discontinuous Galerkin methods (see [4, 12] for instance, see also [11] for cell-centred Galerkin methods). In practice, the penalty parameter η scales as $\eta = \beta\mu$ where μ is the second Lamé coefficient of the material and β is a dimensionless factor that remains user-dependent. In the following, the values $\beta = 1$ and $\beta = 2$ will be used following the numerical experiments performed in [22].

3.4 Verification test case

This section presents a verification test case related to the convergence rate with a singularity at the crack tip. The crack does not propagate, i.e., we consider a steady setting using the above discrete stiffness bilinear form and load linear form. The penalty parameter is chosen as $\eta = \mu$ for this test case. The convergence rate of the method in the presence of a singularity is tested in the case of an infinite plate under mode 3 loading at infinity as presented in Figure 4. A convergence rate of $O(h^{\frac{1}{2}})$, similar to that obtained with Lagrange P^1 finite elements, is expected. The reference solution, close to the crack tip ($\frac{r}{a} \ll 1$), reads in polar coordinates [19, p. 28]:

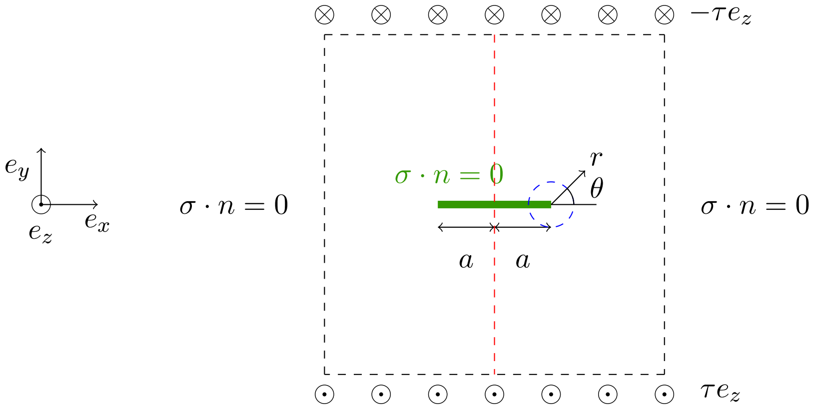

Figure 4: Sketch of the antiplane shear experiment in an infinite plate.

$$u(r,\theta) = \frac{2\tau}{\mu}\sqrt{\frac{ar}{2}}\sin\left(\frac{\theta}{2}\right)e_z, \tag{25}$$

where τ is the modulus of the antiplane shear stress imposed at infinity. The displacement defined in (25) verifies the statics equation in a strong form since $\mathrm{div}(u) = 0$. The stresses are

$$\sigma(r,\theta) = \tau\sqrt{\frac{a}{2r}}\left[\sin\left(\frac{\theta}{2}\right)e_r - \cos\left(\frac{\theta}{2}\right)e_\theta\right] \otimes e_z. \tag{26}$$

Figure 4 being symmetric with respect to the red dashed line, only the right part of the domain is considered. As the analytical solution (25) is only valid close to the crack tip, a small ball around the crack tip, which corresponds to the green dashed circle in Figure 4, is meshed. The setting is presented in Figure 5. The convergence towards the analytical solution is checked on

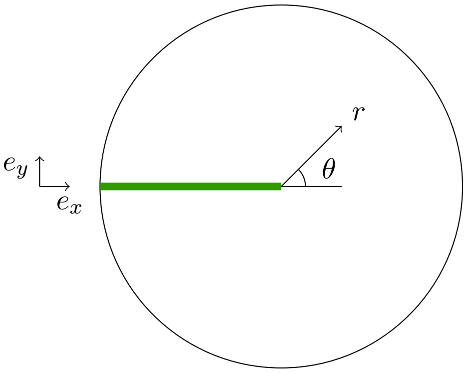

Figure 5: Sketch of the meshed ball around the crack tip.

the meshed ball with the reference solution imposed as Dirichlet boundary condition over the whole boundary including the crack lips. The results of the computation, which are are reported in Table 1, corroborate an $O(h^{\frac{1}{2}})$ convergence rate on the energy-norm, as expected. We also observe an $O(h^{\frac{3}{2}})$ convergence rate on the L^2-norm. The convergence rates are approximated as

nb dofs	$\|u - \mathfrak{R}(u_h)\|_{L^2}$	Convergence rate	$\|\nabla u - G_h(u_h)\|_{L^2}$	Convergence rate
444	5.86e-05	-	1.22e-01	-
$1,776$	1.80e-05	1.70	8.22e-02	0.56
$7,104$	5.87e-06	1.61	5.70e-02	0.53
$28,416$	2.00e-06	1.56	3.98e-02	0.52
$113,664$	6.97e-07	1.52	2.80e-02	0.51

Table 1: Number of dofs, L^2-error and convergence rate, L^2-error on the gradient and convergence rate.

$$\text{order} = d \log\left(\frac{e_1}{e_2}\right)\left(\log\left(\frac{n_2}{n_1}\right)\right)^{-1}, \tag{27}$$

where e_1, e_2 denote the errors on the computations with mesh sizes h_1, h_2 and the number of dofs n_1, n_2.

4 Quasi-static crack propagation

In this section we formulate the discrete problem for quasi-static crack propagation. The space discretization is achieved by means of the DEM scheme presented in the previous section. At every pseudo-time node t_k, the problem is solved iteratively with inner iterations enumerated by $0 \leq m \leq M$. Since the crack can change at each inner iteration, we use the notation $\Gamma_h(t_{k,m})$ for the crack and the notation $\mathcal{F}^i(t_{k,m})$ and $\mathcal{F}^b(t_{k,m})$ for the partition of the mesh facets at the inner iteration m, with the facets located in the crack collected in the subset $\mathcal{F}^\Gamma(t_{k,m})$.

Each inner iteration consists in two steps. First, freezing the position of the crack, we find the discrete displacement $u_h(t_{k,m}) \in V_{hD}(t_k)$ solving the quasi-static problem $a_h(t_{k,m}; u_h(t_{k,m}), \tilde{v}_h) = l_h(t_k; \tilde{v}_h)$ for all $\tilde{v}_h \in V_{h0}$. Then we use the newly computed displacement field $u_h(t_{k,m})$ to determine whether crack propagation occurs and update accordingly the subsets $\mathcal{F}^i(t_{k,m+1})$, $\mathcal{F}^b(t_{k,m+1})$, and $\mathcal{F}^\Gamma(t_{k,m+1})$. We iterate this procedure until there is no more crack propagation in the second step. The inner iteration in the discrete quasi-static crack propagation scheme can thus be summarized as follows: For all $m \in \{0, \dots, M\}$,

$$\begin{cases} \text{(i)} \;\; u_h(t_{k,m}) \in V_{hD}(t_k) \text{ s.t. } a_h(t_{k,m}; u_h(t_{k,m}), \tilde{v}_h) = l_h(t_{k,m}; \tilde{v}_h), \;\; \forall \tilde{v}_h \in V_{h0}, \\ \text{(ii)} \;\; (\mathcal{F}^\Gamma(t_{k,m+1}), \mathcal{F}^b(t_{k,m+1}), \mathcal{F}^i(t_{k,m+1})) = \texttt{CRACK\_QS}(\mathcal{F}^\Gamma(t_{k,m}), \mathcal{F}^b(t_{k,m}), \mathcal{F}^i(t_{k,m}), u_h(t_{k,m})). \end{cases} \tag{28}$$

The rest of this section is devoted to the description of the procedure `CRACK_QS`. This procedure consists in three consecutive steps outlined in Figure 6. The first step involves the procedure `ESTIMATE` which considers all the vertices of $\mathcal{F}^\Gamma(t_{k,m})$ and computes for each of these vertices an approximate energy release rate. The second step involves the procedure `MARK` which flags among all the inner facets sharing a vertex with an energy release rate larger than the maximum value $\mathcal{G}_c$ the facet that will indeed break. The selection is made by using a discrete kinking criterion. The last step uses the procedure `UPDATE` and simply consists in updating the data structure according to the crack propagation. The procedure is repeated from the recomputation of the solution of the first line of Equation (28) until no facet is marked in the procedure `MARK`.

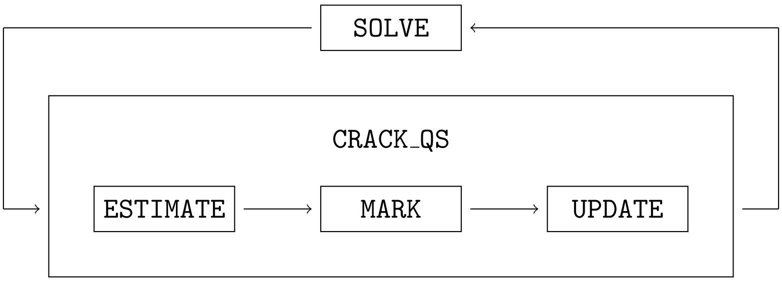

Figure 6: Details of the procedure `CRACK_QS`.

4.1 Procedure `ESTIMATE`

Let $\mathcal{V}^\Gamma(t_{k,m})$ be the set of all vertices in the crack $\Gamma(t_{k,m})$. The procedure `ESTIMATE` computes an approximate energy release rate $\mathcal{G}_h(v)$ for all $v \in \mathcal{V}^\Gamma(t_{k,m})$. Let $\mathcal{F}^\Gamma_{\mathbf{v}}(t_{k,m})$ be the set of cracked facets sharing a vertex $\mathbf{v} \in \mathcal{V}(t_{k,m})$. (The set $\mathcal{F}^\Gamma_{\mathbf{v}}(t_{k,m})$ reduces to a single facet if $\mathbf{v}$ is the crack tip.) Let $\mathcal{F}^i_{\mathbf{v}}(t_{k,m})$ be the set of inner facets sharing a vertex $\mathbf{v} \in \mathcal{V}(t_{k,m})$. An approximate energy release rate for the vertex $\mathbf{v} \in \mathcal{V}(t_{k,m})$ is evaluated as

$$\mathcal{G}_h(\mathbf{v}) := \max_{F \in \mathcal{F}^\Gamma_{\mathbf{v}}(t_{k,m})} \max_{F' \in \mathcal{F}^i_{\mathbf{v}}(t_{k,m})} \pi n_F \cdot \{\Sigma_h(t_{k,m})\}_F \cdot [u_h(t_{k,m})]_{F'}, \tag{29}$$

where $[u_h]_F := u_{c_-} - u_{c_+}$ $\{\Sigma_h\}_F := \frac{1}{2}(\Sigma_{c_-} + \Sigma_{c_+})$, and n_F is the normal vector to F. This expression is rooted in the fact that the elastic energy contained in a facet F writes $\frac{1}{2} n_F \cdot \{\Sigma_h(t_{k,m})\}_F \cdot [u_h(t_{k,m})]_F |F|$ as motivated in [22]. The factor π comes from the fact that the density of elastic energy per facet must be multiplied by 2π to take into account the surface created by cracking (see [19, p. 48]). This is linked to the concept of the crack closure integral. The output of the procedure `ESTIMATE` is the collection of approximate energy release rates $\{\mathcal{G}_h(\mathbf{v})\}_{\mathbf{v} \in \mathcal{V}^\Gamma(t_{k,m})}$.

4.2 Procedure `MARK`

The goal of the procedure `MARK` is to identify the unique inner facet $\mathfrak{F} \in \mathcal{F}^i(t_{k,m})$ through which the crack will propagate. The criterion is based on an adaptation of the maximisation of the strain energy density which was introduced in [28]. Let us first mark the vertices in $\mathcal{V}^\Gamma(t_{k,m})$ whose approximate energy release rate is larger than the material parameter $\mathcal{G}_c$:

$$\mathcal{V}^{\Gamma *}(t_{k,m}) := \{\mathbf{v} \in \mathcal{V}^\Gamma(t_{k,m}), \mathcal{G}_h(\mathbf{v}) \geq \mathcal{G}_c\}. \tag{30}$$

Among all $\mathbf{v} \in \mathcal{V}^{\Gamma *}(t_{k,m})$, we select the single vertex through which the crack will propagate at $t_{k,m}$ as

$$\mathbf{z} := \mathop{\mathrm{Argmax}}_{\mathbf{v} \in \mathcal{V}^{\Gamma *}(t_{k,m})} \mathcal{G}_h(\mathbf{v}). \tag{31}$$

If there is more than one maximizer, one is picked randomly. Having selected the vertex $\mathbf{z}$, we now mark one facet $\mathfrak{F} \in \mathcal{F}^i_{\mathbf{z}}(t_{k,m})$ for cracking. We impose two restrictions on the selection process of the facet to be broken: we limit the number of facets broken per cell to one, and the facet to be broken $\mathfrak{F}$ must locally be in traction which translates into checking only those facets $F \in \mathcal{F}^i_{\mathbf{z}}(t_{k,m})$ such that $[u_h(t_{k,m})]_F \cdot n_F > 0$. The limit of one broken facet per cell is justified by the fact that when a facet breaks, the resulting geometric singularity creates very high stresses that lead to breaking the other facets of the cells containing the facet thus creating many fragments. The limitation we impose is to avoid this situation. The setting is illustrated in Figure 7. The output of the procedure `MARK` is the facet $\mathfrak{F}$, through which the crack will propagate, defined as

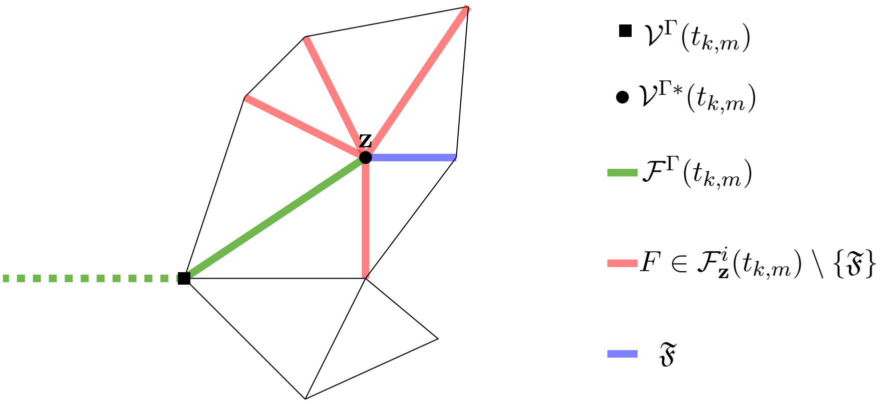

Figure 7: Sketch of the discrete sets considered in the procedure `MARK`.

$$\mathfrak{F} := \mathop{\mathrm{Argmax}}_{\substack{F \in \mathcal{F}^i_{\mathbf{z}}(t_{k,m}) \setminus \mathcal{F}^i_{\mathcal{C}}(t_{k,m}) \\ [u_h(t_{k,m})]_F \cdot n_F > 0}} \frac{1}{2} \{\Sigma_h(t_{k,m})\}_F \cdot \{\varepsilon_h(t_{k,m})\}_F, \tag{32}$$

where $\mathcal{F}^i_{\mathcal{C}}(t_{k,m})$ denotes the set of inner facets contained in a cell with one facet already broken. Note that in most situations, the facet $\mathfrak{F}$ is located at the crack tip.

4.3 Procedure `UPDATE`

The subsets $\mathcal{F}^{\Gamma}(t_{k,m+1})$, $\mathcal{F}^{i}(t_{k,m+1})$, and $\mathcal{F}^{b}(t_{k,m+1})$ can now be updated as follows:

$$\begin{cases} \mathcal{F}^{\Gamma}(t_{k,m+1}) := \mathcal{F}^{\Gamma}(t_{k,m}) \cup \{\mathfrak{F}\}, \\ \mathcal{F}^{i}(t_{k,m+1}) := \mathcal{F}^{i}(t_{k,m}) \setminus \{\mathfrak{F}\}, \\ \mathcal{F}^{b}(t_{k,m+1}) := \mathcal{F}^{b}(t_{k,m}) \cup \{\mathfrak{F}_-, \mathfrak{F}_+\}, \end{cases} \tag{33}$$

where we recall that $\mathfrak{F}_-$ and $\mathfrak{F}_+$ are the same geometric object as the inner facet $\mathfrak{F}$, but are now each one on the boundary of a single mesh cell.

Remark 1 (Update of a_h). *The updates in (33) affect the reconstruction operator used to evaluate the discrete stiffness bilinear form. Figure 8 presents a sketch of an inner facet whose reconstruction has to be recomputed after a neighbouring inner facet breaks. The purpose of recomputing the reconstruction on certain inner facets is to avoid using dof values on both sides of the crack in the same reconstruction.*

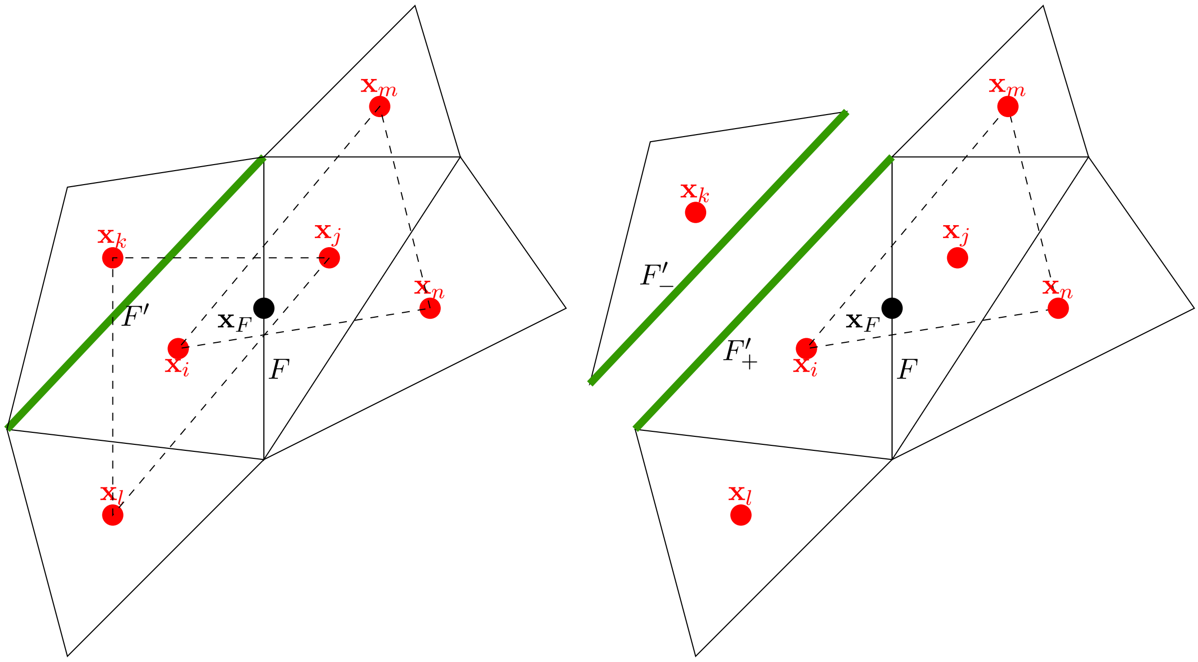

Figure 8: Recomputation of the reconstruction stencil associated with the inner facet F after the breaking of the neighbouring inner facet F'. Left: reconstruction before cracking. Right: reconstruction after cracking. (The two cells separated by the crack are drawn slightly apart.)

5 Numerical experiments

Several numerical experiments are presented to show the versatility of the proposed numerical method.

5.1 Crack speed with prescribed crack path

We consider a test case taken from [21]. The test case consists of an already cracked plate under antiplane shear loading. The crack is forced to propagate along a straight line represented by the dashed line in Figure 9. The goal of this test case is to study the crack propagation velocity. The dimensions of the plate are $L = 5\text{m}$ and $H = 1\text{m}$ and the initial length of the crack is $l_0 = 1\text{m}$. The constant increment in boundary loading is written Δu_D. The material parameters are $\mu = 0.2\text{Pa}$ and $\mathcal{G}_c = 0.01\text{kN/mm}$. The penalty parameter is chosen as $\eta = \mu$. We are interested in the length of the crack with respect to the cumulated boundary loading displacement u_D, where the final displacement load is $u_D = 1\text{m}$. The reference solution for the crack speed S with respect to the loading speed, taken from [21], is $\sqrt{\frac{\mu H}{\mathcal{G}_c}} \approx 4.47$. As this solution is only valid when $L \to \infty$, we checked that doubling the length L of the strip did not lead to any significant

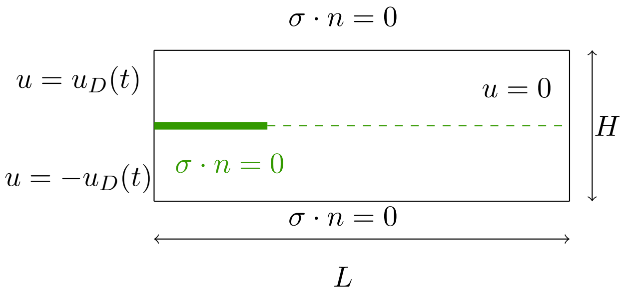

Figure 9: Crack speed: problem setup.

change in the crack speeds. The computations are performed with two structured 2d meshes of triangles with characteristic sizes $h = 5\text{cm}$ and $h = 2.5\text{cm}$. Various values of Δu_D are used in the two computations. Figure 10 reports the crack length as a function of the cumulated loading displacement u_D. One can see that the results with the two meshes are very similar.

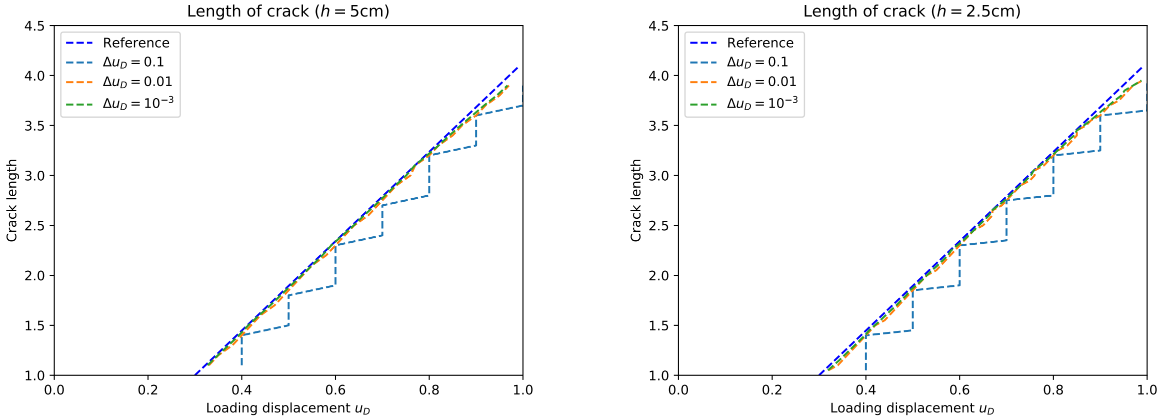

Figure 10: Crack speed: crack length as a function of loading displacement u_D. Left: coarse mesh. Right: fine mesh.

The results with $\Delta u_D = 10^{-3}\text{m}$ and $\Delta u_D = 10^{-2}\text{m}$ are very similar and are in agreement with the analytical solution. For these two values, $\frac{\Delta u_D}{h}$ is less than 0.2 so that the increment in the imposed Dirichlet condition is (much) smaller than the mesh size. This is not the case for $\Delta u_D = 10^{-1}\text{m}$. The different aspect of the curves for $\Delta u_D = 0.1\text{m}$ is explained by the fact that as Δu_D is large in that case, a large number of facets break at each displacement increment thus leading to this staircase shape. However, one can notice that at the end of each displacement increment, the curve for $\Delta u_D = 0.1\text{m}$ reaches the same value as the curves computed with the other Δu_D values. Table 2 contains the errors of the crack speeds (computed with a least-squares fit on the two numerical computations) with respect to the analytical solution. The agreement of the computed crack speeds with the analytical solution is very satisfactory for all Δu_D.

Δu_D / h	0.1	0.05
0.1	2.6%	2.6%
0.01	1.3%	0.74%
0.001	1.4%	0.77%

Table 2: Crack speed: error with respect to analytical solution depending on the choice of h and Δu_D.

5.2 Opening mode with unknown crack path

The setting for this test case is presented in Figure 11. The dimensions of the plate are $L = 32\text{mm}$ and $H = 16\text{mm}$ and the initial length of the crack is $l_0 = 4\text{mm}$. The material parameters chosen are $E = 3.09\text{GPa}$, $\nu = 0.35$ and $\mathcal{G}_c = 300\text{kN/mm}$. The penalty parameter is chosen as $\eta = 2\mu$. First, we use a structured mesh of size $h = 0.4\text{mm}$ containing $25,920$ dofs. The increment in boundary conditions is defined as $\Delta u_D = h$. Figure 12 presents the obtained crack path. We notice an unstable crack propagation, as expected, in the sense that when the propagation starts, it breakes the entire sample at a given t_k. We also perform computations on two unstructured meshes of sizes $h = 1.4\text{mm}$ and $h = 0.74\text{mm}$ corresponding respectively to $2,792$ dofs and $11,044$ dofs. Both meshes do not contain facets with a direction that could lead to a totally straight

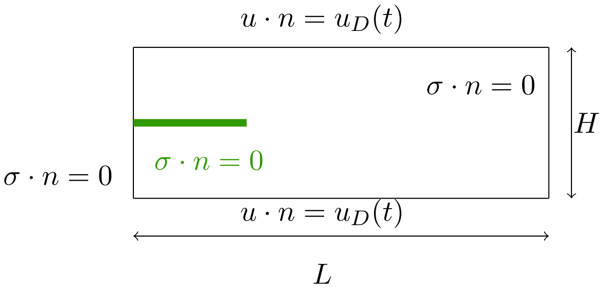

Figure 11: Opening mode: setup.

Figure 12: Opening mode: u_y in colors and crack path in white on a structured mesh.

propagation of the crack. The finer mesh is not a refinement of the coarser one. Figure 13 shows the crack paths obtained on the two meshes. The crack paths obtained are satisfactory as the propagation is rather straight and the results on the two meshes are quite similar.

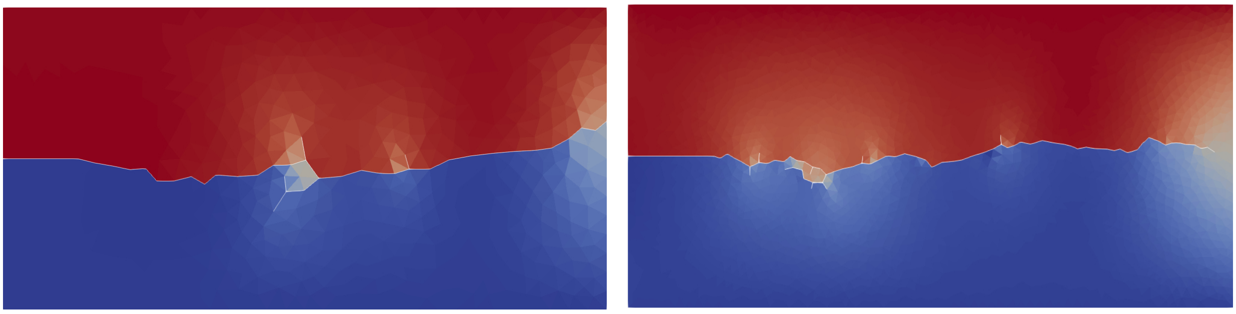

Figure 13: Opening mode: u_y in colors and crack path in white on a unstructured mesh. Left: coarse mesh. Right: fine mesh.

5.3 Single-edge notched shear test

The setting of this test case comes from [1]. It consists in a square with an already initiated crack loaded in shear on its top surface. The lower surface is recessed while the upper surface is loaded in shear. The two lateral parts are free of stress as well as the crack. Figure 14 illustrates the setting. The crack is of initial length $l_0 = 0.5$mm and the dimension of the sample is $H = 1$mm. The material parameters are $E = 210$GPa, $\nu = 0.3$ and $\mathcal{G}_c = 2.7 \cdot 10^{-3}$kN/mm. The increment of boundary load is defined as $\Delta u_D = 10^{-6}$mm and the final load is $u_{D,\text{final}} = 0.02$mm. The penalty parameter is chosen as $\eta = 2\mu$.

Three computations are performed on unstructured meshes of size $h = 6.9 \cdot 10^{-5}$m, $h = 2.6 \cdot 10^{-5}$m and $h = 1.6 \cdot 10^{-5}$m having respectively $2,140$, $16,640$ and $44,446$ dofs. Figure 15 shows the commuted crack paths. Our results can be compared with [26] which uses a phase-field model discretized by a hybridizable discontinuous Galerkin formulation. The computations are

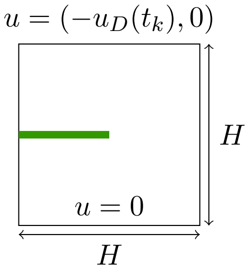

Figure 14: Single-edge notched shear test: setup.

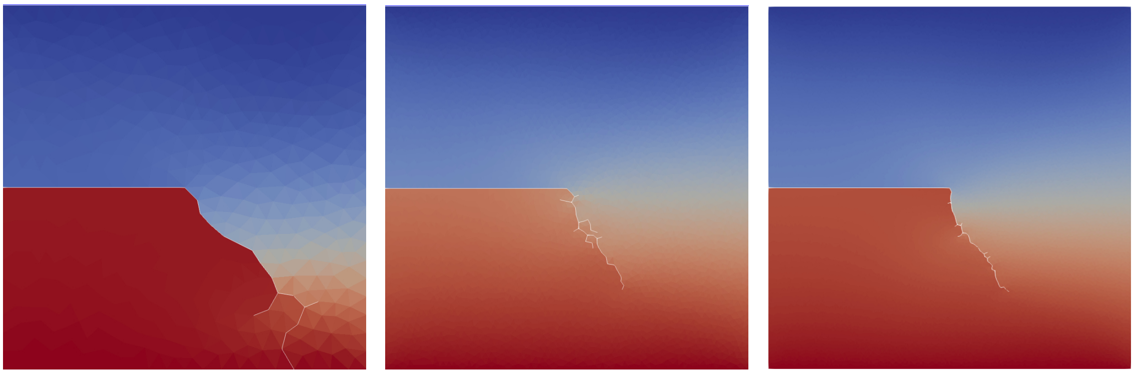

Figure 15: Single-edge notched shear test: u_x in colors and crack path in white. Left: coarse mesh. Middle: fine mesh. Right: finest mesh.

in agreement with the computation of [26] regarding the general orientation of the crack and the number of branches.

5.4 Notched plate with a hole

This test case comes from [6]. The material parameters are $E = 6\text{GPa}$, $\nu = 0.22$, and $\mathcal{G}_c = 2.28 \cdot 10^{-3}\text{kN/mm}$. We use fixed displacement increments of $\Delta u_D = 10^{-2}\text{mm}$. The penalty parameter is chosen as $\eta = 2\mu$. Figure 16 presents a sketch of the sample. The dimensions of the plate are $L = 65\text{mm}$ and $H = 120\text{mm}$. The two holes on the left of the sample have a diameter of 10mm and the hole on the right of the sample has a dimeter of 20mm. The initial length of the crack is $l_0 = 10\text{mm}$. One also has $a = 20\text{mm}$, $b = 55\text{mm}$, $d = 69\text{mm}$ and $e = 36.5\text{mm}$. The right hole is free of stress, the lower hole is recessed and the upper hole has an imposed displacement $u = (0, u_D(t_k))$. The final displacement is $u_{D,\text{final}} = 1\text{mm}$. We use

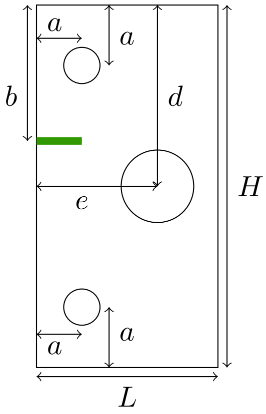

Figure 16: Notched plate with a hole: setup.

three unstructured meshes with $h = 6.6$mm, $h = 2.1$mm and $h = 1.5$mm having respectively $1,976$, $19,010$ and $39,504$ dofs. Figure 17 shows the computed crack paths. We compare our results with [26] without taking into account the secondary crack starting from the largest hole as we restrict ourselves to crack propagation and not crack initiation. We notice that for the three computations, the crack goes towards the largest hole in a similar fashion which also seems consistent with [26].

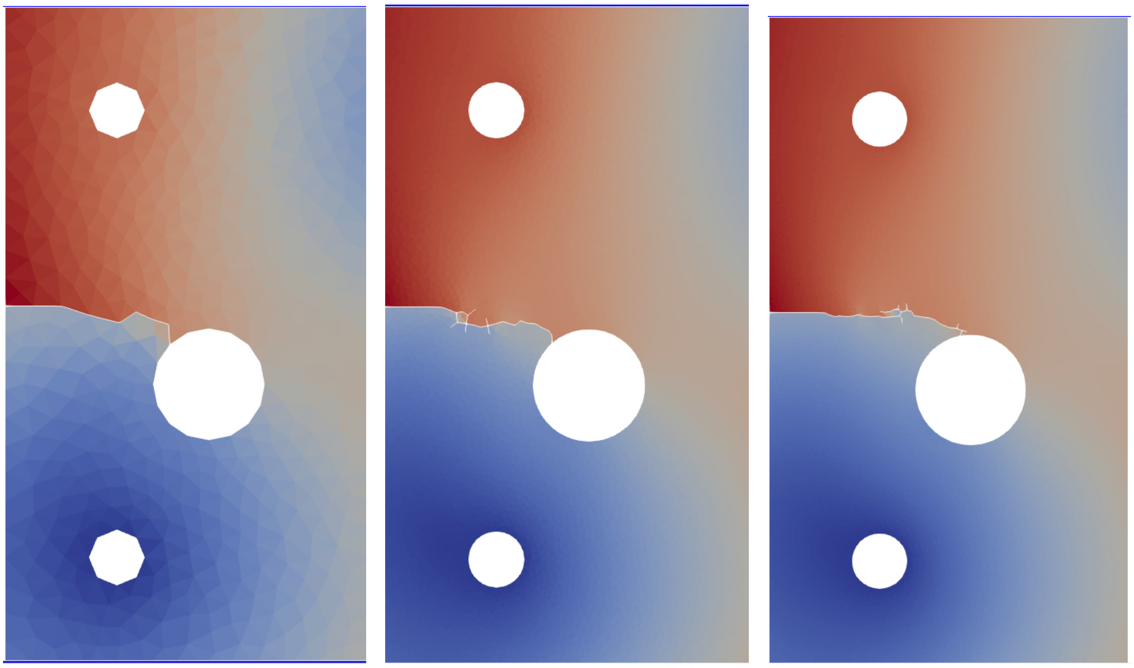

Figure 17: Notched plate with a hole: u_y in colors and crack path in white. Left: coarse mesh. Middle: fine mesh. Right: finest mesh.

6 Conclusion

We have presented a Discrete Element Method (DEM) to compute Griffith crack propagation. The crack propagates through the facets of the mesh and thus between discrete elements. The DEM is a consistent discretization of a Cauchy continuum and only requires continuum macroscopic parameters such as the Young modulus and the Poisson ratio for its implementation. The displacement degrees of freedom are attached to the barycentre of the mesh cells and to the barycentre of the Dirichlet boundary facets. A discrete Stokes formula is used to devise a piecewise constant gradient and linearized strain reconstructions. An approximation of the energy release rate has been devised in the procedure `ESTIMATE`. A procedure `MARK` has been devised to determine the breaking facet at each pseudo-time node t_k. Finally, the procedure `UPDATE` has been devised to update the necessary discrete quantities after the facet that has been marked has been broken. A convergence test in antiplane shear has confirmed the efficiency of the DEM discretization as well as the $\mathcal{O}(h^{\frac{1}{2}})$ convergence rate in energy norm. The robustness of the method regarding the computation of the crack speed has been verified. Also, several numerical experiments have shown that the method can provide reasonable crack paths.

This work can be pursued in several directions. A first idea would be to adapt the present methodology to three-dimensional problems with two-dimensional cracks. A second direction concerns the regularity of the crack surface. Indeed, in the spirit of [14], a crack should be a surface that minimizes energy. To achieve this goal, the DEM could be coupled to gradient flows used for surface lifting, as in [27], with the goal of moving the crack surface vertices. One would then have to verify the convergence of the discrete crack area with tools similar to [16]. A third direction for further study is to approximate cohesive cracking laws instead of a Griffith cracking law so as to enable the simulation of crack initiation as well as crack propagation. Inspiration can be found in [23] which is DEM with a linear cohesive law. Finally, a last direction can be to consider an enrichment similar to [9] close to the crack tip so as to obtain a convergence with order $\mathcal{O}(h)$.

Acknowledgements

Partial support by CEA is gratefully acknowledged.

References

[1] M. Ambati, T. Gerasimov, and L. De Lorenzis. A review on phase-field models of brittle fracture and a new fast hybrid formulation. *Comput. Mech.*, 55(2):383–405, 2015.

[2] D. André, J. Girardot, and C. Hubert. A novel DEM approach for modeling brittle elastic media based on distinct lattice spring model. *Comput. Methods Appl. Mech. Eng.*, 350:100–122, 2019.

[3] D. André, M. Jebahi, I. Iordanoff, J.-L. Charles, and J. Néauport. Using the discrete element method to simulate brittle fracture in the indentation of a silica glass with a blunt indenter. *Comput. Methods Appl. Mech. Eng.*, 265:136–147, 2013.

[4] D. Arnold. An interior penalty finite element method with discontinuous elements. *SIAM J. Numer. Anal.*, 19(4):742–760, 1982.

[5] T. Belytschko, Y. Y. Lu, and L. Gu. Element-free Galerkin methods. *Int. J. Numer. Methods Eng.*, 37(2):229–256, 1994.

[6] M. Borden, C. Verhoosel, M. Scott, T. Hughes, and C. Landis. A phase-field description of dynamic brittle fracture. *Comput. Methods Appl. Mech. Eng.*, 217:77–95, 2012.

[7] B. Bourdin, G. A. Francfort, and J.-J. Marigo. Numerical experiments in revisited brittle fracture. *J. Mech. Phys. Solids*, 48(4):797–826, 2000.

[8] M. A. Celigueta, S. Latorre, F. Arrufat, and E. Oñate. Accurate modelling of the elastic behavior of a continuum with the discrete element method. *Comput. Mech.*, 60(6):997–1010, 2017.

[9] E. Chahine, P. Laborde, and Y. Renard. Crack tip enrichment in the XFEM using a cutoff function. *Int. J. Numer. Methods Eng.*, 75(6):629–646, 2008.

[10] G. Dal Maso. Generalised functions of bounded deformation. *J. Eur. Math. Soc.*, 15(5):1943–1997, 2013.

[11] D. A. Di Pietro. Cell centered Galerkin methods for diffusive problems. *ESAIM. M2AN*, 46(1):111–144, 2012.

[12] D. A. Di Pietro and A. Ern. *Mathematical aspects of discontinuous Galerkin methods*, volume 69. Springer Science & Business Media, 2011.

[13] R. Eymard, T. Gallouët, and R. Herbin. Discretization of heterogeneous and anisotropic diffusion problems on general nonconforming meshes SUSHI: a scheme using stabilization and hybrid interfaces. *IMA J. Numer. Anal.*, 30(4):1009–1043, 2009.

[14] G. A. Francfort and J.-J. Marigo. Revisiting brittle fracture as an energy minimization problem. *J. Mech. Phys. Solids*, 46(8):1319–1342, 1998.

[15] P. Hansbo and K. Salomonsson. A discontinuous Galerkin method for cohesive zone modelling. *Finite Elem. Anal. Des.*, 102:1–6, 2015.

[16] K. Hildebrandt, K. Polthier, and M. Wardetzky. On the convergence of metric and geometric properties of polyhedral surfaces. *Geometriae Dedicata*, 123(1):89–112, 2006.

[17] A. Hussein, B. Hudobivnik, F. Aldakheel, P. Wriggers, P.-A. Guidault, and O. Allix. A virtual element method for crack propagation. *PAMM*, 18(1):e201800104, 2018.

[18] M. Jebahi, D. André, I. Terreros, and I. Iordanoff. *Discrete element method to model 3D continuous materials.* John Wiley & Sons, 2015.

[19] M. Kuna. *Finite elements in fracture mechanics.* Springer, 2013.

[20] C. Labra and E. Oñate. High-density sphere packing for discrete element method simulations. *Commun. Numer. Methods Eng.*, 25(7):837–849, 2009.

[21] T. Li, J.-J. Marigo, D. Guilbaud, and S. Potapov. Numerical investigation of dynamic brittle fracture via gradient damage models. *Adv. Model. Simul. Eng. Sci.*, 3(1):26, 2016.

[22] F. Marazzato, A. Ern, and L. Monasse. A variational discrete element method for quasistatic and dynamic elastoplasticity. *Int. J. Numer. Methods Eng.*, 121(23):5295–5319, 2020.

[23] C. Mariotti, V. Michaut, and J.-F. Molinari. Modeling of the fragmentation by discrete element method. In *DYMAT 2009 9th Int. Conf. Mechanical and Physical Behaviour of Materials under Dynamic Loading*, pages 1523–1528, 2009.

[24] N. Moës and T. Belytschko. X-FEM, de nouvelles frontières pour les éléments finis. *Revue européenne des Eléments*, 11(2-4):305–318, 2002.

[25] L. Monasse and C. Mariotti. An energy-preserving discrete element method for elastodynamics. *ESAIM. M2AN*, 46:1527–1553, 2012.

[26] A. Muixí, A. Rodríguez-Ferran, and S. Fernández-Méndez. A hybridizable discontinuous galerkin phase-field model for brittle fracture with adaptive refinement. *Int. J. Numer. Methods Eng.*, 121(6):1147–1169, 2020.

[27] P. Romon. *Introduction à la géométrie différentielle discrète.* Ellipses, 2013.

[28] G. C. Sih. Strain-energy-density factor applied to mixed mode crack problems. *International Journal of fracture*, 10(3):305–321, 1974.

[29] L. Simon. Lectures on geometric measure theory. In *Proceedings of the Centre for Mathematical Analysis, Australian National University*, volume 3. Australian National University Centre for Mathematical Analysis, Canberra, 1983.

[30] M. Spellings, R. L. Marson, J. A. Anderson, and S. C. Glotzer. GPU accelerated discrete element method (DEM) molecular dynamics for conservative, faceted particle simulations. *J. Comput. Phys.*, 334:460–467, 2017.

[31] N. Sukumar, B. Moran, T. Black, and T. Belytschko. An element-free Galerkin method for three-dimensional fracture mechanics. *Comput. Mech.*, 20(1-2):170–175, 1997.